RESEARCH ARTICLE

Parallel imaging in non-bijective, curvilinear magnetic field gradients: a concept study

**Juergen Hennig · Anna Masako Welz ·
Gerrit Schultz · Jan Korvink · Zhenyu Liu ·
Oliver Speck · Maxim Zaitsev**

Abstract

Objectives The paper presents a novel and more generalized concept for spatial encoding by non-unidirectional, non-bijective spatial encoding magnetic fields (SEMs). In combination with parallel local receiver coils these fields allow one to overcome the current limitations of neuronal nerve stimulation. Additionally the geometry of such fields can be adapted to anatomy.

Materials and methods As an example of such a parallel imaging technique using localized gradients (PatLoc)-system, we present a polar gradient system consisting of 2×8 rectangular current loops in octagonal arrangement, which generates a radial magnetic field gradient. By inverting the direction of current in alternating loops, a near sinusoidal field variation in the circumferential direction is produced. Ambiguities in spatial assignment are resolved by use of multiple receiver coils and parallel reconstruction. Simulations demonstrate the potential advantages and limitations of this approach.

Results and conclusions The exact behaviour of PatLoc fields with respect to peripheral nerve stimulation needs to be tested in practice. Based on geometrical considerations SEMs of radial geometry allow for about three times faster gradient

J. Hennig (✉) · A. M. Welz · G. Schultz · M. Zaitsev
Department of Diagnostic Radiology, Medical Physics,
University Hospital, Hugstetterstr.55, 79106 Freiburg, Germany
e-mail: juergen.hennig@uniklinik-freiburg.de

J. Korvink · Z. Liu
Department of Microsystem Engineering,
Laboratory for Simulation, Freiburg, Germany

O. Speck
Faculty for Natural Sciences,
Otto-von-Guericke University Magdeburg,
Magdeburg, Germany

switching compared to conventional head gradient inserts and even more compared to whole body gradients. The strong nonlinear geometry of the fields needs to be considered for practical applications.

Introduction

Conventional magnetic resonance imaging employs temporally and spatially variable magnetic fields to encode position by the local Larmor frequency of spins. Gradient systems used for that purpose are designed to produce spatially linearly varying fields (=constant gradients) in three orthogonal directions *x, y, z*. Such constant gradients lead to a direct mapping of the local resonance frequencies to spatial coordinates such that an image without distortions is produced after Fourier transformation of the time domain signals. Constant gradients have the benefit of constant voxel size and signal intensities across the image can be directly compared without the need for any volumetric correction. In addition, the use of constant gradients to encode physical parameters, such as flow or diffusion, allows for isotropic parameter encoding. Linearity is, therefore, a high priority in the design of gradient systems. To achieve gradients with defined amplitude and slew rate in practice; however, a compromise has to be made between linearity and efficiency of gradients, since the demand for high linearity leads to designs requiring high voltage and currents. More important, at the current stage of development, gradient system performance for MRI is limited by safety concerns due to peripheral nerve stimulation (PNS) rather than by technical limitations of gradient coils and/or power supplies [1,2]. Peripheral nerve stimulation increases with the local rate of change of the magnetic

field. The maximum stimulation is induced at the location of the largest field amplitude ΔB_{max} generated by the gradient coil. ΔB_{max} and consequently the most severe rate of field change $\Delta B_{max}/dt$ is located outside of the constant gradient field and scales with the size of the gradient system for a given gradient field geometry and slew rate. For a given limit of $\Delta B_{max}/dt$, a higher slew rate can only be achieved with smaller gradient systems.

We have begun to explore the possibility of non-Cartesian gradient encoding in the context of the recently proposed one voxel one coil (OVOC) approach, which is based on the use of spatial sensitivity profiles of multiple small coils as primary source for spatial localization [3]. A similar approach has been called inverse MR imaging [4]. As already shown in the application for high temporal resolution mapping of brain physiology [3] additional spatial information at least in one spatial direction can be introduced by one-dimensional encoding with a gradient in a suitable direction. In the context of this application it would be desirable to orient the direction of spatial encoding along the surface of the cortex (radial or circumferential) rather than in Cartesian coordinates x, y and z. In this paper we will present basic concepts of the use of gradients with radial symmetry for imaging.

Methods

Since the term 'gradients' is firmly ingrained to represent constant gradients in Cartesian coordinates, and also to avoid confusion with the usage of the term 'gradient' as the spatial derivative of the main magnetic field B_0, we use the term spatial encoding magnetic field (SEM) for the general case of non-Cartesian spatially variable fields. In general SEMs with spherical or cylindrical geometry include multiple field maxima and minima. Using such SEMs for spatial encoding, thus, leads to a non-bijective correlation between frequency domain and the location in object space. Therefore spatial encoding is inherently ambiguous. Unambiguous encoding is constrained to local subregions of the SEMs. The global ambiguity can be resolved by parallel imaging approaches using multiple local receiver coils. The number nc of coil elements has to be equal to or larger than the degree of ambiguity of the spatial encoding. We use the term parallel imaging technique using local gradients (PatLoc) for this approach.

Arrangements of arrays of planar coils derived from a three rung Cho design were used to generate the desired PatLoc fields [5]. A radial gradient can be achieved by placing ng such coils along the circumference of a cylinder. In order to extend the radial field in the z-direction, a head-to-head arrangement of two coils was used as the basic building block as suggested in [5]. The distance between the six central rungs was 8 mm, respectively, the length in z-direction was 80 mm at 40 mm width. Figure 1 shows an octagonal arrangement of such coils.
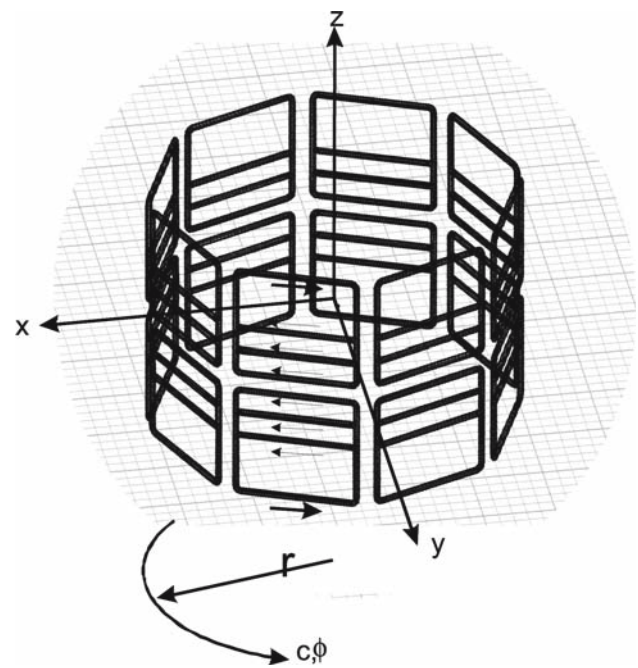

Fig. 1 Octagonal coil arrangement used in the simulations. 2×8 planar coils are arranged in an octagonal arrangement around the direction of the main field (z). r and ϕ denote the radial resp. azimuthal directions in polar coordinates. *Arrows* next to the rungs indicate the current direction

Magnetic field simulations were performed using a MatLab software package (Mathworks Natick, MA, USA) for solving the Biot-Savart law for one-dimensional current distributions on a cylinder. The program was adapted from MatLab code developed by Fa-Hsuan Lin at MGH available on the internet (http://www.nmr.mgh.harvard.edu/~fhlin/tool_b1.htm). For refinements the designs were transferred into Maxwell3D (AnSoft Inc, Pittsburgh, PA, USA) for FDTD-calculations based on realistic materials and geometries (copper wire with 2 mm thickness, rounded corners). The maximum deviation between the idealized Biot-Savart calculations and the Ansoft simulation was ~5% close to the wire. For simulations of SEMs for imaging the analysis was applied to the central plane, where concomitant fields can be ignored due to the symmetry of the arrangement. The field profile along the z-direction leads to a reduction in the maximum amplitude of B_z to 98.5, 92.2, 79.2 and 55% at 1, 2, 3 and 4 cm off-center in the z-direction, respectively.

Simulations of the one-dimensional signal behavior were performed by using equidistant vectors of magnetization. Typically between 64 and 256 isochromats per pixel and 1,024 pixels were used to avoid discretization artifacts. T_2^*-decay as well as other physical parameters affecting the signal were ignored.

For two-dimensional signal behavior 16×16 isochromats per pixel were used in order to keep the matrix size and calculation times within a reasonable range for use with MatLab. Simulation results show that beyond 4×4 isochromats per pixel there is no significant change in results.

Simulations

Figure 2 shows a radial field generated by a current $I = 10$ A through each of the 2×3 rungs of the SEM coil elements. The return path (larger arrow in Fig. 1) through the outer rungs carried 30 A on each side. The radius of the cylindrical coil array was assumed to be 6 cm, which corresponded to the target size aimed for in a first technical implementation. The field profile in the radial direction is shown in Fig. 3a and b displays the gradient in the radial direction. Figure 3b reveals that the local gradient along r is identical to the mean gradient located at a position 57% outwards from the center. For a given bandwidth and resolution in the frequency domain such a SEM will thus lead to higher spatial resolution towards the periphery of the SEM, whereas spatial resolution will deteriorate towards the center. To evaluate the SEM performance regarding spatial resolution and localization, a simulation was performed using a one-dimensional periodic spin density distribution. The period of the modulation pattern was 4 pixels (peak-to-peak) at a halfwidths of approximately 1 pixel. The pattern was generated by starting with a periodic grid of deltafunctions, which was low pass filtered to the desired halfwidth and convolved with a bell-shaped filter to reduce ringing artifacts. Halfwidth was chosen to be sufficiently narrow in order to demonstrate some blurring at the mean gradient amplitude. A constant average gradient G_{const} of 9.11 mT/m as shown in Fig. 3a was applied with data acquisition with a bandwidth of 40.96 kHz and a resolution of 160 Hz/pixel. Sixty-four equidistant spins per pixel were used in the simulation to yield a total of 256×64 isochromats. For each isochromat a signal was calculated according to its Larmor frequency (Fig. 4a). The halfwidth
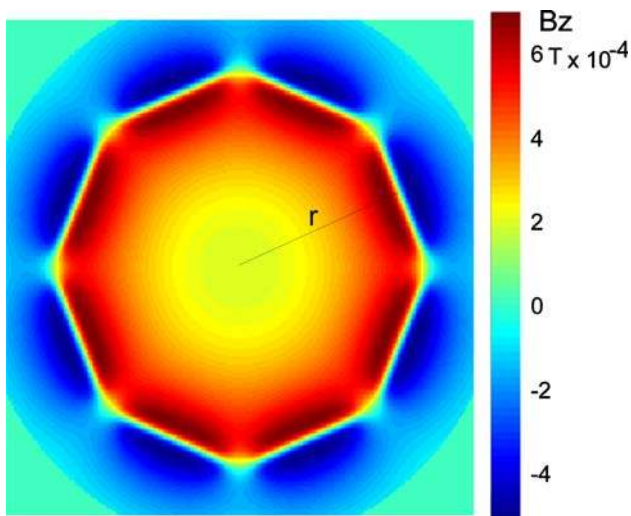

Fig. 2 A color-coded field plot of magnetic field B_z produced by the coil array in (Fig. 1) with a current of 10 A through each of the six rungs at the center of the planar coils at a radius $r = 6$ cm. The maximum field is 0.68 mT at a radius $r = 5.56$ cm from the center
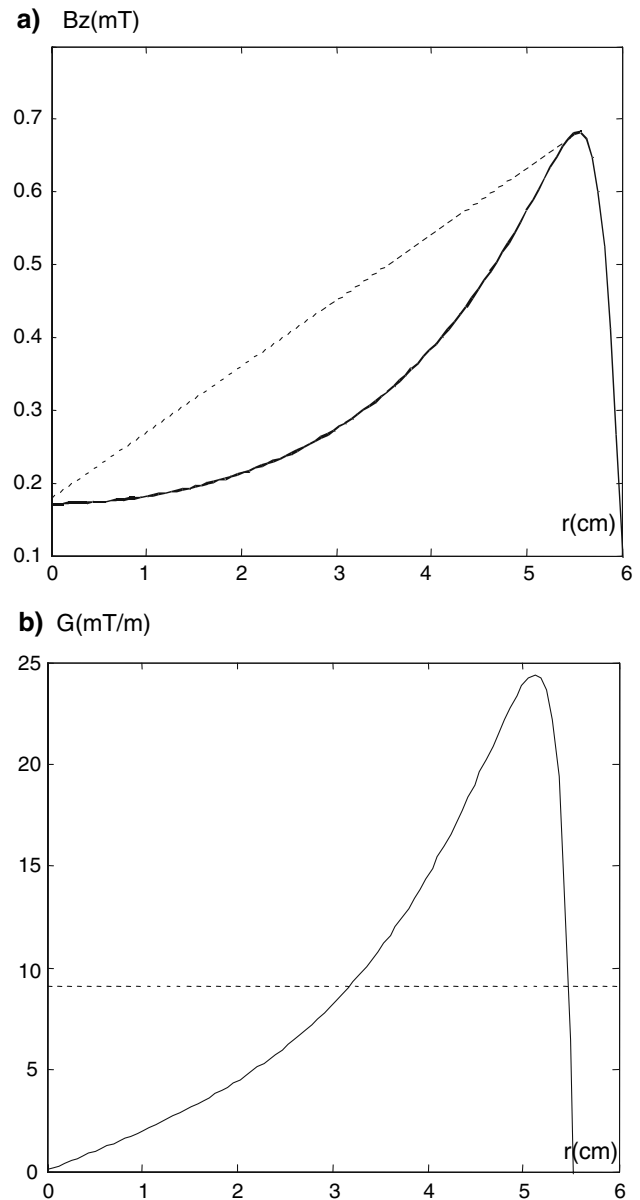

Fig. 3 **a** Field Bz along r. The *dotted line* represents a constant gradient with identical maximum and minimum. **b** Gradient G corresponding to the derivative of Bz along *r*. The *dotted line* represents the mean gradient between the field maximum and minimum

of the observed modulation pattern is ~ 2 pixels. For display the signal was interpolated to 2,048 points by zerofilling to avoid partial volume effects.

Figure 4b shows the spectrum of the same periodic one-dimensional spin density distribution consisting of 256 pixels, when brought into a one-dimensional radial SEM_R aligned along r in Fig. 2 with a field and gradient profiles as shown in Fig. 3. In order to avoid foldover artifacts, the spin density outside of the field maximum (at $r = 5.53$ cm in Fig 3a) was set to zero. Retransformation into spatial coordinates (Fig. 4c) reveals the higher resolution of the PatLoc
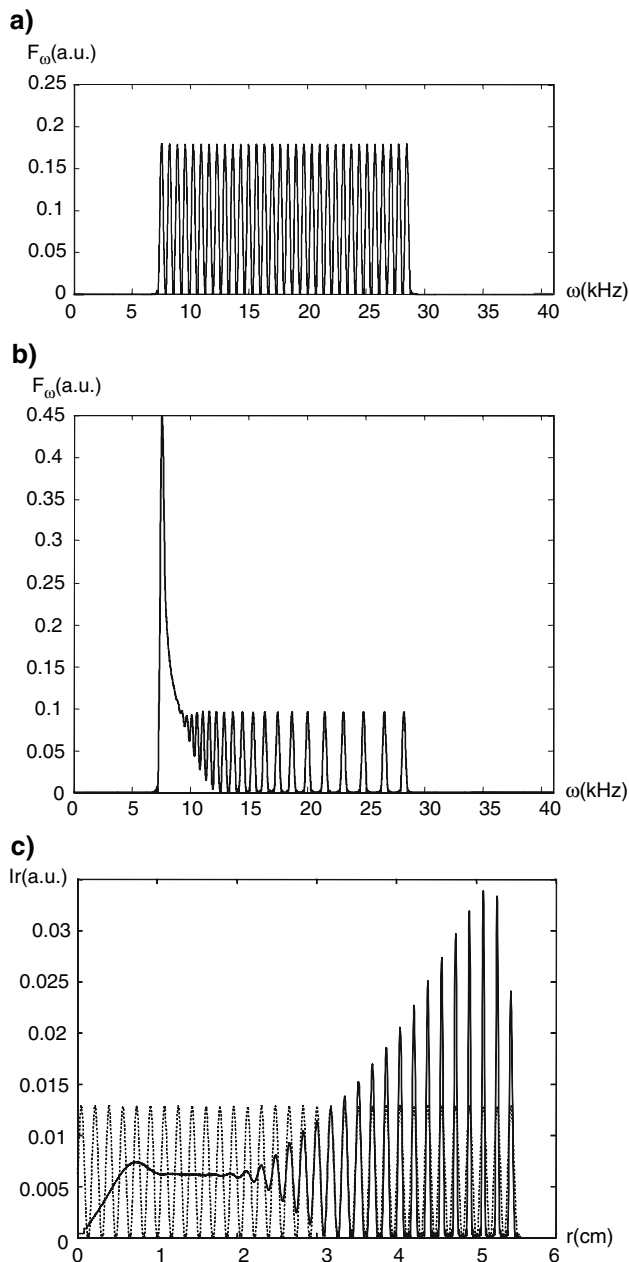
a)

b)

c)

Fig. 4 **a** Spectrum $F\omega$ of a periodically modulated spin distribution with a peak-to-peak distance of 4 pixels and ∼1 pixel halfwidth measured with a constant mean gradient G_{const} at a bandwidth $\omega = 40,960$ Hz. The observed halfwidth of the spectrum is ∼2 pixels. **b** Spectrum $F\omega$ of same spin distribution observed in the radial SEM_R shown in Fig. 3b at identical bandwidth. **c** Spectra from **a** and **b** mapped to spatial coordinates

a)

b)

Fig. 5 **a** Magnetic field profile of SEM_C generated from an octopole arrangement of coils with a current of 10 A flowing in alternating directions through the coil configuration shown in Fig. 1. *Arrows* indicate the primary direction of the field gradient. The wedge shaped outline shows one of the eight subregions for unambiguous (*but curved*) spatial encoding. **b** Gradient of the SEM_C at equidistant positions in the dotted ring shown in (Fig. 5a) as a function of the azimuth angle ϕ. Only two of the four gradient lobes ($0 < \phi < 180°$) are shown for clarity

encoding at larger r with a cross-over at a position, where SEM_R equals G_{const}. The integral over each peak is constant; therefore, the peak amplitudes are increased at increased resolution.

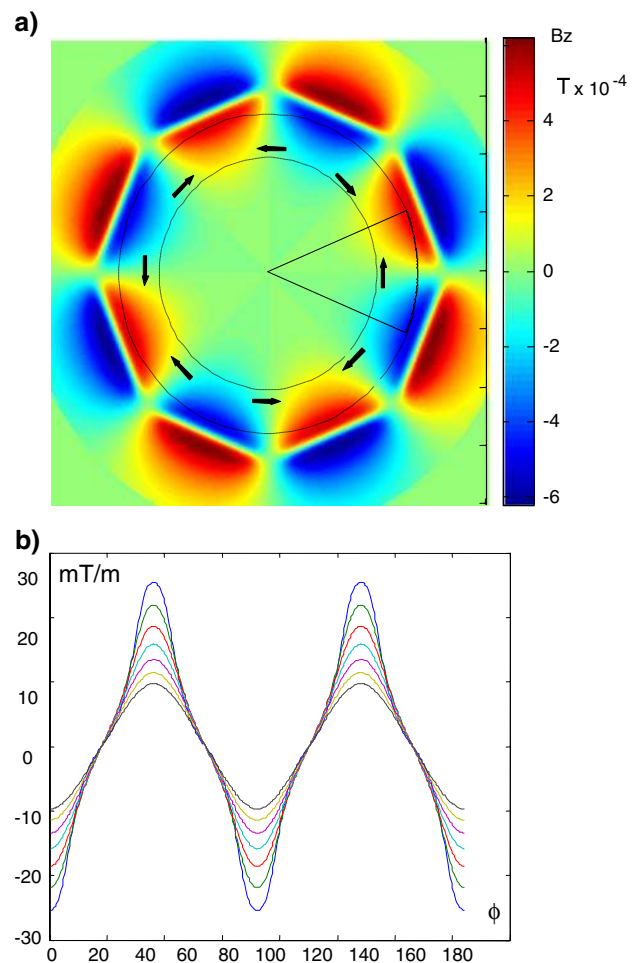If the proposed SEM_R is used as readout gradient, an additional SEM_C with a circumferential gradient is required to achieve two-dimensional image encoding. However, such circumferential gradients are fundamentally impossible to realize in a monotonic fashion [6]. In addition to physical constraints set by Maxwell's equations the circumferential field will thus be multipolar by necessity. A didactically interesting and very straightforward, but in practice not necessarily optimal approach to establish a multipolar circumferential SEM_C is achieved by alternating the current in the coil elements of the radial SEM_R. The resultant octopole field profile is shown in Fig. 5a. Figure 5b shows the gradient $dBz/dc = 1/r \ dBz/d\phi$ in the circumferential direction c normal to the radius r along the azimuth coordinate ϕ at radii 4, 4.25, ..., 5.5 cm. Compared to the radial SEM_R (Fig. 3b) the maximum amplitude of the circumferential SEM_C is increased, but decays more rapidly towards the center due to interference between the opposing field lobes.

Fig. 6 Basic workflow for PatLoc reconstruction of a spin distribution $I_\rho(x, y)$ into its PatLoc image $I_{xy}(x, y)$. For explanation see text
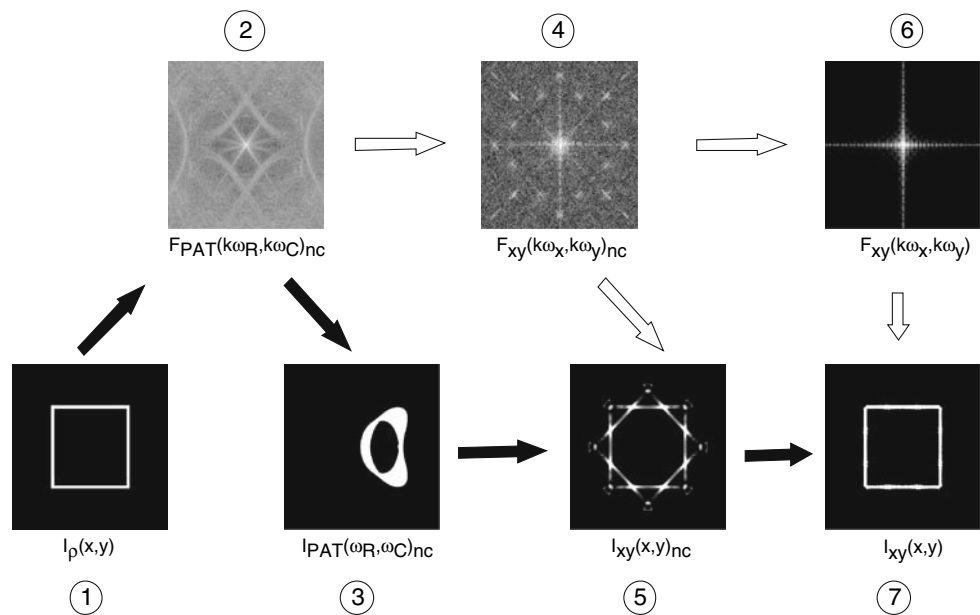
Using SEM_R and SEM_C for 2D-imaging requires modification of the usual reconstruction pipeline. The basic workflow of the reconstruction algorithm is shown in Fig. 6. The black arrows indicate the pathway used in our simulations: a given spin distribution $I_\rho(x, y)$ (Fig 6, 1) results in a k-space dataset $F_{PAT}(k\omega_R, k\omega_C)_{nc}$ (Fig 6, 2) for each of the nc receiver coils. Each dataset represents the signals acquired by using SEM_R and SEM_C for two-dimensional Fourier encoding: 2DFT will transform $F_{PAT}(k\omega_R, k\omega_C)_{nc}$ from frequency space into $I_{PAT}(\omega_R, \omega_C)_{nc}$ (Fig 6, 3) where ω_R, ω_C are defined by the Larmor frequencies at each point in the fields generated by SEM_R and SEM_C. For known field profiles of the SEMs, $I_{PAT}(\omega_R, \omega_C)_{nc}$ can be transformed into Cartesian coordinates to yield $I_{xy}(x, y)_{nc}$ (Fig. 6, 5): ω_R and ω_C are linked to x, y by

$$\omega_R = \gamma B_{SEMR}(x, y) \qquad (1)$$

and

$$\omega_c = \gamma B_{SEMC}(x, y) \qquad (2)$$

where B_{SEMR} and B_{SEMC} correspond to the fields generated by the two SEMs.

Coordinate transformations are performed by calculating the inverse functions of (1) and (2). Since (1) and (2) are non-bijective, the inverse will lead to ambiguous mapping of $I_{PAT}(\omega_R, \omega_C)_{nc}$ to $I_{xy}(x, y)_{nc}$. For the practical implementation the inverse function was calculated numerically: for each Cartesian coordinate (x,y) the (ω_R, ω_C)-coordinates were derived from (1) and (2) and the signal intensity was calculated from $I_{PAT}(\omega_R, \omega_C)_{nc.}$ using regridding with linear interpolation.

The resulting image $I_{xy}(x, y)_{nc}$ demonstrates an eightfold degeneracy due to the ambiguity of spatial encoding in the multipolar fields. Based on the known sensitivity profiles of each of the nc receiver coils the true image $I_{xy}(x, y)$ (Fig. 6, 7) can be unwrapped by generalizing and adapting SENSE reconstruction [7] or refinements thereof [8]. Alternatively, warping of $F_{PAT}(k\omega_R, k\omega_C)_{nc}$ into Cartesian k-space $F_{xy}(k\omega_x, k\omega_y)nc$ (Fig. 6, 4) can be performed using a transformation matrix based on the shift theorem. Data can then be combined by a GRAPPA type of parallel reconstruction [9,10] into Cartesian k-space (Fig. 6, 6). The final image (Fig. 6, 7) is then reconstructed by 2DFT.

In order to avoid additional complexity from idiosyncrasies and imperfections of the parallel reconstruction algorithms, i.e., to remove the effects of the RF coil sensitivities, we have used eight idealized wedge-shaped coil profiles (see Fig. 5a) in our simulations. In this very artificial setup the coil sensitivity is one within each wedge and zero outside. An image can then be generated by performing a simple addition of the individual coil images by simple PILS recombination [11]. For display all images were expanded to $1{,}024 \times 1{,}024$ matrix size by sinc-interpolation.

In order to illustrate the imaging behavior for PatLoc encoding (Fig. 7) shows a direct comparison of simulated patterns for conventional gradients and encoding with SEM_R and SEM_C, respectively. The amplitude of the conventional gradients was assumed to be equal to the mean gradient amplitude of B_{SEMR} as shown in Fig. 3a. In order to avoid ambiguities and, therefore, foldover in the radial direction, the field-of-view was limited to 5.5 cm such that both PatLoc gradients decay monotonously towards the center.

The circular pattern consisting of rings of finite widths (Fig. 7a, b) demonstrates the higher resolution of PatLoc

Fig. 7 Results of simulations of circular (**a, b**), spokewheel (**c, d**) and random (**e, f**) spin distribution patterns imaged by constant Cartesian gradients (*left column*) versus PatLoc gradients SEM_C and SEM_R (*right column*). Linewidth of the modulated geometrical patterns was roughly 1 pixel at 256×256 matrix size
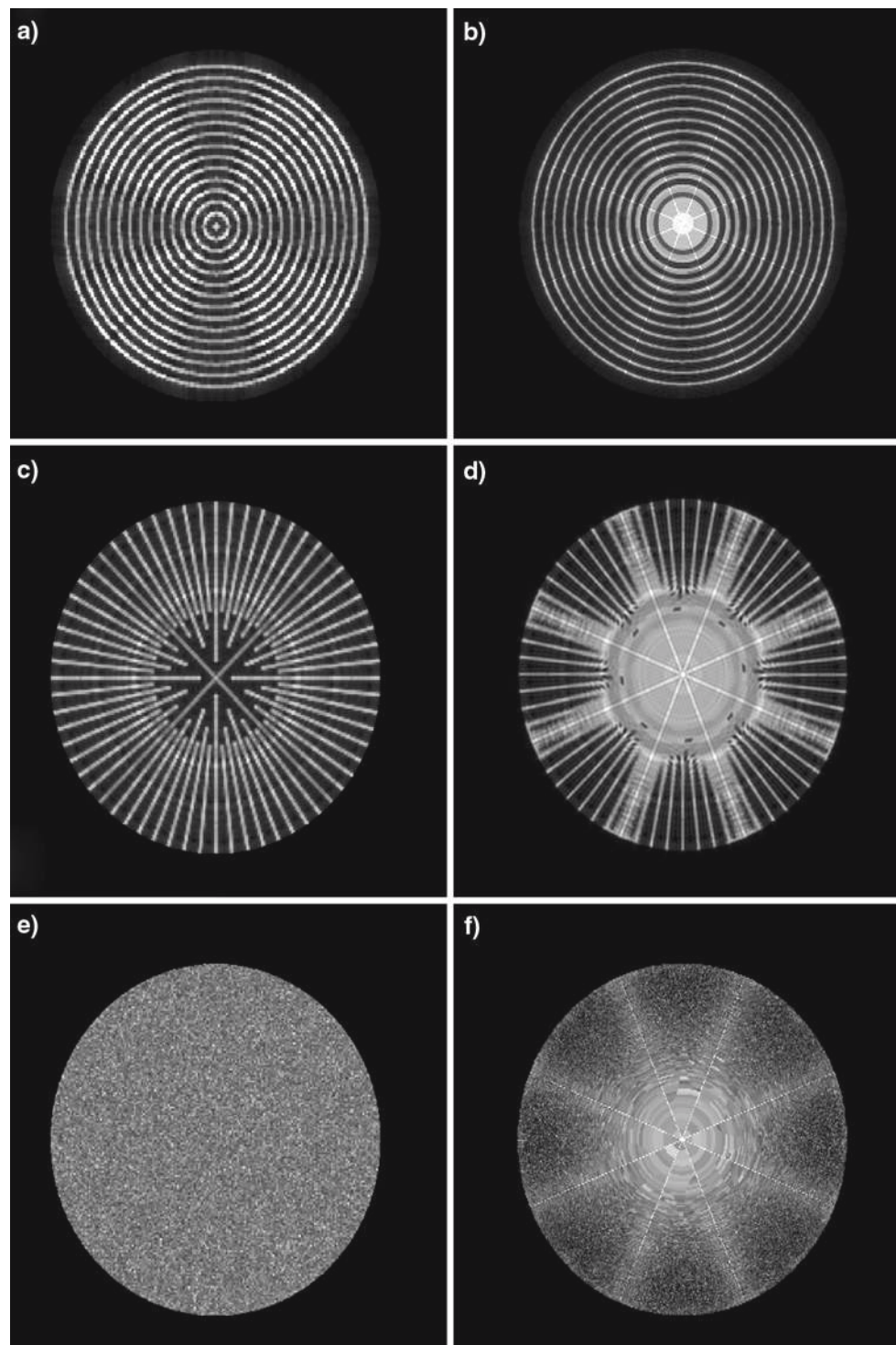
encoding towards the rim of the pattern as well as the widening of the rings towards the center. Simulated images of a radial spoke wheel pattern (Fig. 7c, d) show the circumferential variation of the image resolution as a consequence of the smoothness of the gradient near the field maxima and minima (see Fig. 5b).

Simulations of regular but non-linear discrete structures can be misleading due to regridding artifacts and mathematical singularities near the field maxima and minima. Loss of resolution at areas of low and/or non-orthogonal gradient fields also appears to be rather patchy leading to enlarged patchy areas more than to blurring. This is most likely a

consequence of the simulation using a large but still finite number of isochromats where the intensity of isochromats within each pixel is constant. For a realistic situation with a homogeneous distribution of uncorrelated spins smooth blurring is expected in areas of low spatial resolution.

In addition to using regular structures we have thus used a 'noise image' generated by a random distribution of spin density in Cartesian space to visualize the overall transformation characteristics. An overall impression of the anisotropic imaging behavior is shown in Fig. 7f. Substantial blurring near the image center can clearly be identified. In addition, degraded image quality is visible near eight spokes at azimuthal positions corresponding to the gradient minima and non-orthogonal (or even parallel) gradient directions of B_{SEMR} and B_{SEMC}..

In order to analyze the impact of such effects on a more realistic case, we have used a standard MR-image as template for the spin distribution. A 512×512 image of a human volunteer rescaled to the size of the gradient bore was used as a model for $I\rho(x, y)$ and 'imaged' with conventional gradients versus PatLoc gradients. As illustrated in Fig. 8, image resolution of the PatLoc image is clearly degraded towards the center of the head. In contrast good image quality can be seen at the outer cortex close to the 'spokes' indicating the minima and maxima of SEMs or vanishing local gradients if data are acquired at 384×384 resolution (Fig. 8b). At 256×256 image resolution (Fig. 8c) the appearance of the angular blurring is more pronounced.

The circumferential anisotropy could be compensated for by repeating the experiment using the radial SEM_R and an interleaved circumferential SEM_{CI}, where SEM_{CI} is derived from SEM_C by a rotation of $22.5°$. In practice, however, such an approach would double the acquisition time. An alternative strategy to improve rotational anisotropy is to directly use SEM_C and SEM_{CI} for spatial encoding. The orientation of the gradient fields produced by both SEM_C and SEM_{CI} changes continuously over space. Field direction is radial along the radii connecting the extremity and circumferential halfway between. In view of this continuous swirling around it is remarkable that the gradient fields are homogeneously orthogonal across the entire FoV (Fig. 9) with a maximum and minimum crossing angle α of $109.5°$ and $70.2°$, respectively. As shown in simulated images (Fig. 10) this leads to an increase of the extent of the low resolution part at the center due to the more rapid decline of the fields towards the center, but to a beneficial rotational isotropy of the resulting images along the circumference.

Discussion

Although the particular geometry of the SEMs discussed in this paper is novel, there is abundant previous literature
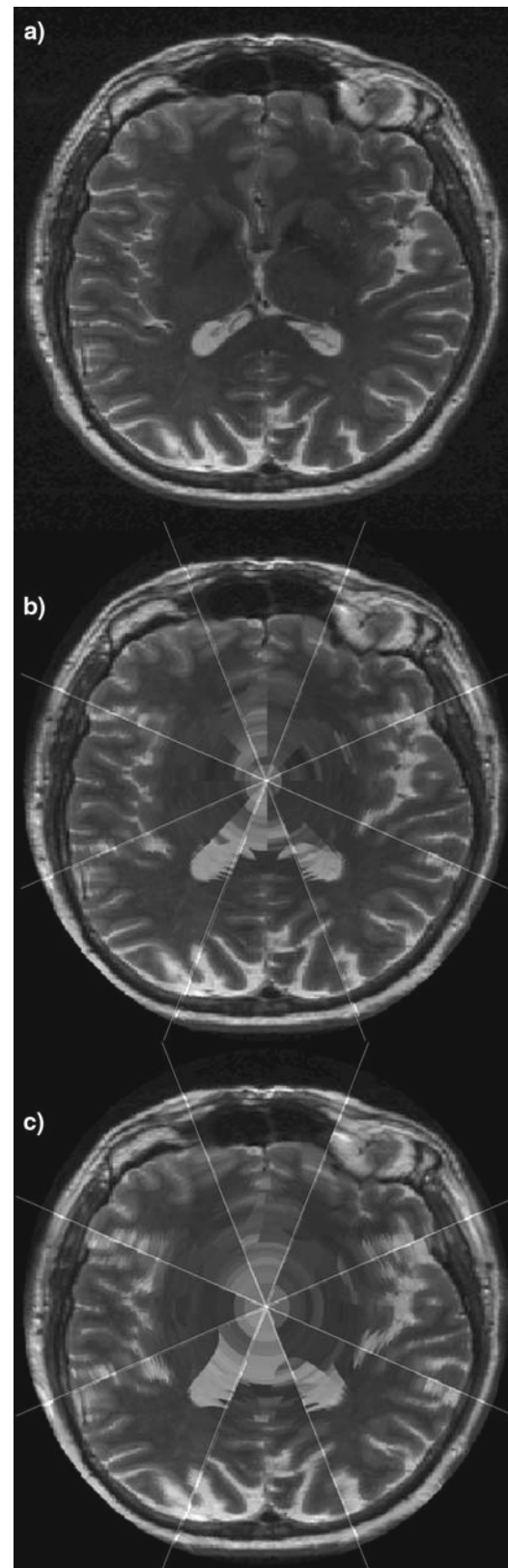

Fig. 8 Spin distribution taken from a 512×512 volunteer image imaged simulated to be imaged with conventional gradients (**a**) and with PatLoc gradients SEM_R and SEM_C acquired at 384×384 (**b**) and 256×256 (**c**) matrix size
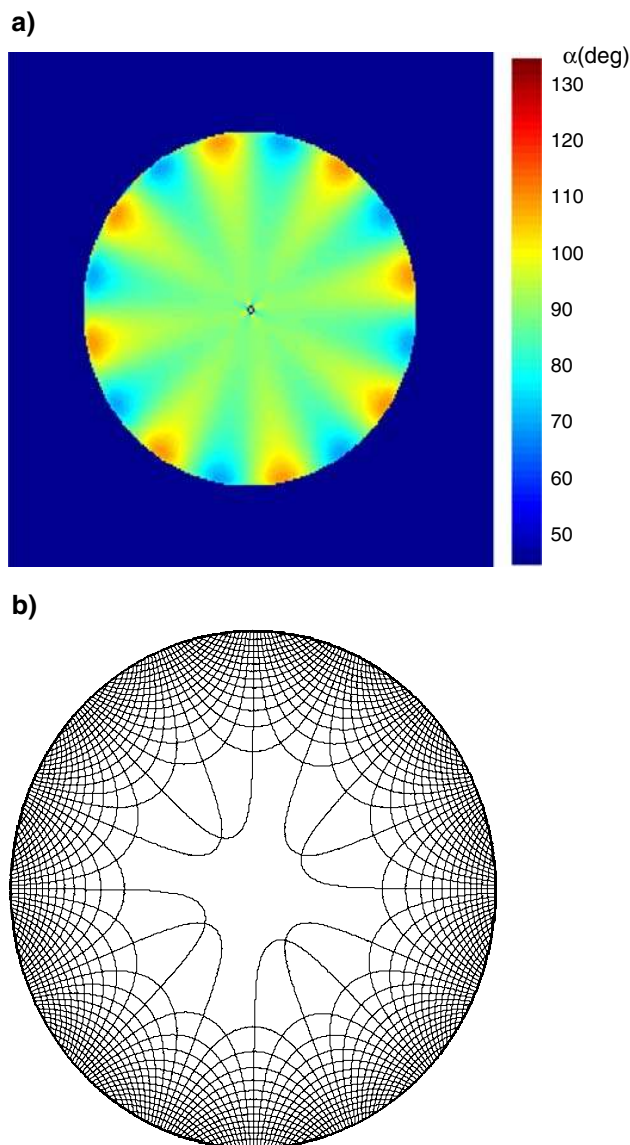
a)

b)

Fig. 9 a Colour encoded display of the angle α between the gradients produced by the multipolar SEM_C and the interleaved multipolar SEM_{CI} generated from SEM_C by rotation by 22.5°. **b** Superposition of isocontour lines of SEM_{CI} and SEM_C

regarding different aspects of PatLoc imaging. Nonlinear spatial encoding fields have found numerous applications outside clinical and biomedical MR. Flat gradient systems [12,13] and inside-out encoding fields [14,15] are well known. In the field of medical MR the use of sinusoidal varying gradients has been described by Patz [16–18]. Recently non-bijective but still unidirectional fields have been suggested, which maintain the orthogonality of conventional gradients [19].

The reconstruction workflow shown in Fig. 6 is formally equivalent to the use of 2DFT with re-warping to account for gradient non-linearities, which is commonly used in most scanners today. In PatLoc imaging nonlinearities can how-

ever not be treated as a simple perturbation any more, but constitute an inherent part of the imaging process. Therefore a number of commonly used concepts which have been developed to guide intuition for conventional imaging need to be reconsidered. Frequency domain and Cartesian space are disjoint in PatLoc imaging, such that basic properties of signal sampling theory in the time/frequency domain cannot be simply translated into imaging properties in spatial coordinates:

The use of a globally constant point spread function (PSF) to characterize the imaging behavior fails. When using PatLoc encoding each pixel has its own PSF reflecting the fact that spins at different spatial positions have different k-space trajectories. Based on the curvature of the SEMs, the PSF of each pixel will be anisotropic with variable preferential directions. As a result spatial resolution will become a local property and can be highly variable across the image.

The field of view (FoV) in conventional imaging is linked to the distance between adjacent samples (a local property) in k-space:

$$FoV = \omega_N/(\gamma G) = 1/(dw\gamma G), \tag{3}$$

where γ is the gyromagnetic ratio, G the gradient and ω_N the Nyquist frequency defined by the sampling rate 1/dw. Application of this interrelationship to local variable gradients produced by SEMs is not correct and implies that the FoV (in spatial coordinates) becomes spatially variable. This somewhat defies intuition, where FoV clearly is perceived as a property of the image as a whole.

So it needs to be noted that basic concepts derived from signal theory like the Nyquist theorem are still applicable to corresponding frequency domains in PatLoc coordinates ((2) and (3) in Fig. 6) but can no longer be directly translated into the spatial domain. Care needs to be taken when translating imaging properties like over- and under-sampling, foldover and others from the frequency domain into spatial coordinates.

The simulation presentd in this study have neglected the influence of physical parameters such as field inhomogeneities, chemical shift effects, T_2^* and others to be accounted for in a real implementation. One may also suspect that the use of idealized wedge shaped sensitivity profiles makes images look better than could be expected in a more realistic situation. For conventional 2DFT sampling strategy based on the use of one SEM as readout gradient and the second as phase encoding gradient, off-resonance effects due to field inhomogeneities will produce a shift in the direction of the local gradient of the SEM used as readout gradient. If SEM_R is used for that purpose, the chemical shift displacement in the final image will increase radially towards the center. For any of the multipole SEMs, the chemical shift displacement will change its direction and extent all over the image. As a result, it can be expected that fat/water-suppression and/or

Fig. 10 Simulation of a phantom image produced by combining the circular and spoke wheel patterns in (Fig. 7a, c) when imaged with conventional gradients and with SEM$_C$ and SEM$_{CI}$. Linewidth of the geometrical patterns was ~ 1 pixel at 256×256 matrix size
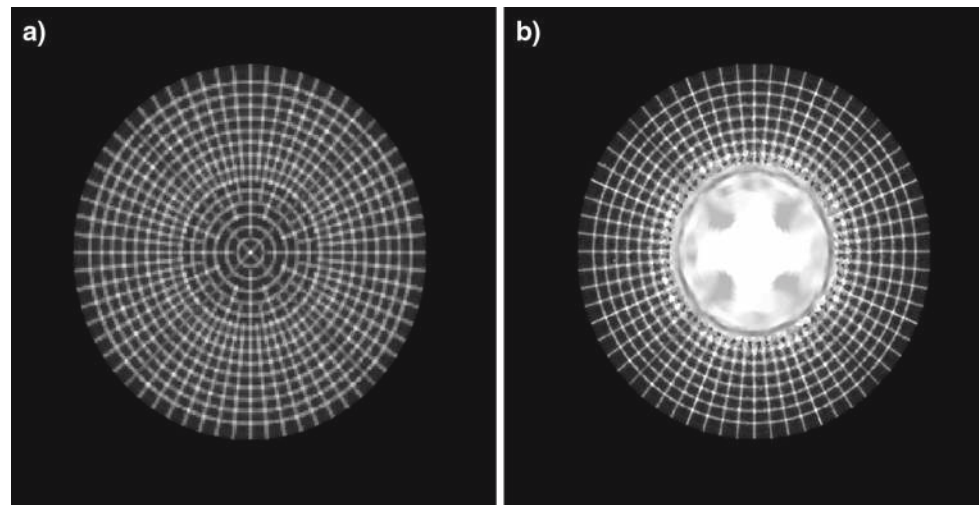
more advanced techniques correcting for local field effects may be mandatory for realistic applications of PatLoc imaging. The complexity will increase with the use of advanced sampling strategies (EPIs, Spirals, VIPR, …) in PatLoc experiments. Effects will be most dramatic near the maxima and minima of the SEM fields, where local gradients are small and changes in signal phase or frequency will result in artifacts across an appreciable distance.

Additional complications are expected, if the information about the position of the probe in the SEM fields is incorrect or if the actual SEM field amplitudes deviate from their nominal value by eddy current effects, or other instabilities.

Apart from the challenges to be met regarding measurement and image reconstruction, building PatLoc systems will be far from trivial. Force and torque issues as well as eddy current problems need to be considered in the practical realization.

The coil arrangement used for generating the SEMs is geometrically different, but in principle similar to coil arrangements used in current shim systems. Time variable switching of high order shims is currently discussed for use in high field imaging and spectroscopy and known to be a difficult, but (hopefully) not insurmountable problem.

External interferences will be much smaller in multipolar coil arrangements. The cylindrical antipolar symmetry of the induced effects is highly self compensating within the cylindrical arrangement of conductive surfaces in current MR systems. The self-compensating nature of mechanical forces over short distances is also promising and may lead to benefits with respect to acoustic noise.

The efficiency of the coils as well as the geometry of the fields can be further optimized using either analytical methods, such as the target field approach [20,21], or by numerical optimization based on FEM- or FDTD-methods [22].

The octagonal arrangement described in this study reflects a compromise between gradient amplitude/slew rate and field-of-view: With increasing number of poles stronger and faster gradients can be realized, but the useful imaging volume is more and more restricted to the rim of the circular FoV.

PatLoc SEMs are not meant to be used as stand-alone devices, but in connection with the still existing conventional gradients. A conventional z-gradient is a natural complement to the multipolar SEMs to extend the measurement region into a cylindrical volume. Slice selection will normally be performed with a conventional gradient in order to select a planar slice of homogeneous thickness. For any combination of PatLoc, SEMs and conventional gradients the mutual non-orthogonality must be taken into account especially outside of the magnet center, where concomitant gradients can be significant.

Similarly, PatLoc SEMs may be useful to increase the flexibility of conventional data acquisition. Using the radial SEM$_R$ for slice selection can be useful to select a circular slice at the center and/or a cylindrical tube as volume of interest, which can then be imaged using conventional imaging techniques. The underlying radial geometry suggests that back-projection techniques will be the natural approach for imaging such volumes. Volumetric applications will be affected by the homogeneity of PatLoc fields along the z-direction.

Using PatLoc SEMs not for imaging but to encode parameters such as flow and diffusion is feasible, but will lead to spatial variation of relevant parameters like venc and b-factors.

Our simulations show that imaging with multipolar SEMs is feasible, but it comes at a price of significant anisotropy characterized especially by a hole at the center of the imaging volume. Given this inherent limitation, one is tempted to ask whether the complexity of the PatLoc encoding approach might outweigh its potential advantages. One incentive already mentioned is the possibility to use the radial SEM for 'depth-encoding' in a OVOC-experiment as in MR-Encephalography.

Our simulations allow some estimates with respect to physiological limitations set by peripheral nerve stimulation (PNS). PNS depends on the local change of dB/dt and the switching time ts [23,24]. Threshold values for PNS are individually variable and may also depend on the exact geometry of the variable fields. For conventional gradients the physiologically relevant ΔB_{max} is located at the periphery or even outside the usable field of view and scales with the size of the gradient system. PatLoc SEMs will lead to considerably reduced ΔB_{max} even at high gradient amplitude due to the alternating nature of the fields between the multiple poles. The relevant 'pole distance' r_{PNS} in conventional gradients defined as the distance between the maximum and minimum field generated by the gradient is at least as large as the diameter $2r$ of the gradient system. In contrast, for an octopole SEM $_C r_{PNS}$ is smaller than $\pi/4r$ due to the fact that the maxima and minima are located inside of the gradient volume. From these geometrical considerations alone one can expect that SEMs allow for considerable faster and/or stronger gradients by approximately a factor of three before the stimulation threshold is reached.

Currently ongoing developments at our institution focus on the demonstration that such a system can be realized in practice and that—most important—useful applications can be developed to exploit the advantages of such an approach.

Since the advent of parallel imaging and more recently receiver coil arrays becoming an integral part of the standard imaging systems the fundamental concept of using homogeneous magnetic field gradients to achieve globally unambiguous spatial encoding was not critically reviewed. Indeed, for unambiguous imaging using a coil array, it is sufficient to achieve reasonably homogeneous encoding over the field of view of each receiver coil. This degree of freedom, relaxing the requirement of global linearity of the encoding fields may in our belief result in numerous advantages in switching speed, nerve stimulation, acoustic properties, etc.

Although it may well be that the radicalness of the approach described in this paper may limit practical applications, we are confident that liberating gradient design from the restrictive requirements regarding linearity may permit realization of more flexible and efficient spatial encoding schemes and may help to drive MR imaging beyond the current physiological limits.

References

1. Schenck JF (2005) Physical interactions of static magnetic fields with living tissues. Prog Biophys Mol Biol 87:185–204
2. Schenck JF (2000) Safety of strong, static magnetic fields. J Magn Reson Imaging 12(1):2–19
3. Hennig J, Zhong K, Speck O (2007) MR-Encephalography: fast multi-channel monitoring of brain physiology with magnetic resonance. Neuroimage 34(1):212–219
4. Lin FH, Wald LL, Ahlfors SP, Hamalainen MS, Kwong KK, Belliveau JW (2006) Dynamic magnetic resonance inverse imaging of human brain function. Magn Reson Med 56(4):787–802
5. Cho ZH, Yi JH (1991) A novel type of surface gradient coil. J Magn Reson 94:471–495
6. Penrose LS, Penrose R (1958) Impossible Objects: A Special Type of Visual Illusion. Brit J Psychology 49:31–33
7. Pruessmann KP, Weiger M, Scheidegger MB, Boesiger P (1999) SENSE: sensitivity encoding for fast MRI. Magn Reson Med 42(5):952–962
8. Larkman DJ, Nunes RG (2007) Parallel magnetic resonance imaging. Phys Med Biol 52(7):R15–R55
9. Griswold MA, Jakob PM, Heidemann RM, Nittka M, Jellus V, Wang J, Kiefer B, Haase A (2002) Generalized autocalibrating partially parallel acquisitions (GRAPPA). Magn Reson Med 47(6):1202–1210
10. Blaimer M, Breuer F, Mueller M, Heidemann RM, Griswold MA, Jakob PM (2004) SMASH, SENSE, PILS, GRAPPA: how to choose the optimal method. Top Magn Reson Imaging 15(4):223–236
11. Griswold MA, Jakob PM, Nittka M, Goldfarb JW, Haase A (2000) Partially parallel imaging with localized sensitivities (PILS). Magn Reson Med 44(4):602–609
12. Vegh V, Zhao H, Galloway GJ, Doddrell DM, Brereton IM (2005) The design of planar gradient coils. Part I: A winding path correction method. Concepts Magn Reson B Magn Reson Eng 27(1):17–24
13. Vegh V, Zhao H, Doddrell DM, Brereton IM, Galloway GJ (2005) The design of planar gradient coils part II: A weighted superposition method. Concepts Magn Reson B Magn Reson Eng 27(1):25–33
14. Cooper RK, Jackson JA (1980) Remote (inside-out) NMR. I. Remote production of a region of homogeneous magnetic field. J Magn Reson 41:400–405
15. Jackson JA, Burnett LJ, Harmon JF (1980) Remote (inside-out) NMR. III. Detection of nuclear magnetic resonance in a remotely produced region of homogeneous magnetic field. J Magn Reson 41:411–421
16. Hrovat MI, Pulyer YM, Rybicki FY, Patz S (1999) Reconstruction algorithm for novel ultrafast MRI. Int J Imaging Syst Technol 10:209–215
17. Patz S, Hrovat MI, Pulyer YM, Rybicki FY (1999) Novel encoding technology for ultrafast MRI in a limited spatial region. Int J Imaging Syst Technol 10:216–224
18. Hrovat MI, Patz S (2006) MRI imaging with a PERL field. US Patent US 6,977,500 B1
19. Parker DL, Hadley JR (2006) Multiple-region gradient arrays for extended field of view, increased performance, and reduced nerve stimulation in magnetic resonance imaging. Magn Reson Med 56(6):1251–1260
20. Turner R (1986) A target field approach to optimal coil design. J Phys D Appl Phys 19:147–151
21. Turner R (1988) Minimum inductance coils. J Phys E Sci Instrum 21:948–952
22. Turner R (1993) Gradient coil design: a review of methods. Magn Reson Imag 11:903–920
23. Reilly JP (1992) Peripheral nerve and cardiac excitation by time-varying magnetic fields: A comparison of thresholds. NY Acad Sci 649:96–117
24. Schaefer DJ, Bourland JD, Nyenhuis JA (2000) Review of patient safety in time-varying gradient fields. J Magn Reson Imaging 12(1):20–9